PERGAMON

International Journal of Solids and Structures 39 (2002) 3599–3623

INTERNATIONAL JOURNAL OF SOLIDS and STRUCTURES

www.elsevier.com/locate/ijsolstr

Foam mechanics: nonlinear response of an elastic 3D-periodic microstructure

Myriam Laroussi [a], Karam Sab [b,*], Amina Alaoui [a]

[a] *LAMI—Ecole Nationale des Ponts et Chaussées, 6 & 8 avenue Blaise Pascal, Cité Descartes, Champs-sur-Marne, 77455 Marne–la–Vallée cedex 2, France*

[b] *LMSGC—2 allée Képler, Champs-sur-Marne, 77420 Marne–la–Vallée, France*

Received 22 February 2002

Abstract

The compressive response of a 3D open-cell foam with periodic tetrakaidecahedral cells is studied through combined theoretical and numerical efforts. Under compressive loading the response is characterized by an extended load plateau following the relatively sharp rise to a maximum load. Several processes of loading have been simulated numerically using appropriately nonlinear kinematics. The onset of failure under macroscopic loading conditions is shown to be the reason of the load plateau. A failure surface is defined in macroscopic stress space by the onset of the first buckling-type instability encountered along proportional load paths. The analysis is carried out through two methods. The first one consists in increasing specimen size with periodic boundary conditions leading to the termed microfailure surface. The second one consists in considering both periodic and nonperiodic displacements variations on a minimum unit cell. The resulting failure surfaces are shown to coincide. Moreover, the postbuckling analysis has been carried out for two particular loadings: the uniaxial compression and the uniaxial deformation.

Keywords: Foam material; Periodic cells; Microstructures; Buckling; Finite strains

1. Introduction

Cellular solids are made up of an interconnected network of cells with solid strut edges. Their cell faces can be open (e.g. open-cell polyurethane), sometimes they are covered by plates or membranes (e.g. closed-cell polyethylene), or both (e.g. polyether foam with both open and closed cells). These materials can be broadly categorized into two groups. The first group, termed ''honeycombs'', consists in cellular materials with a 2D geometric arrangement, while the second group, termed ''foams'', includes those materials with

* Corresponding author. Fax: +33-1-40435450.

E-mail addresses: laroussi@lami.enpc.fr (M. Laroussi), karam.sab@lcpc.fr (K. Sab), alaoui@lami.enpc.fr (A. Alaoui).

0020-7683/02/$ - see front matter
PII: S0020-7683(02)00172-5

fully 3D microstructure. Low density cellular solids (density ratios of the order of 0.02–0.1) are widely used in engineering applications, due mainly to their high stiffness-to-weight ratios. In addition, as they can undergo very large deformations at low stress levels, cellular materials when subjected to compression have excellent shock mitigation and energy absorption characteristics (see Maiti et al., 1984).

Pioneering works on the mechanical properties of cellular materials are those of Gent and Thomas (1963), Shaw and Sata (1966) and Patel and Finnie (1970). The book edited by Hilyard (1982) contains a series of articles which summarize the state of the art (at that period of time) for polymeric foams. Credit for refocusing the attention of the research community to the mechanics of cellular materials must be given to Gibson and Ashby (1988) for their comprehensive study of the structure, the properties and the mechanical behavior of a wide range of honeycombs and foams, both natural and synthetic. The aforementioned works constitute an excellent starting point for any worker in the field. However, due to their broad scope, these investigations do not always address, in depth, the mechanisms involved at the different stages of deformation of such solids. In particular, they didn't give the appropriate emphasis to the crucial role played by instabilities, caused by strong material and geometric nonlinearities, and which lead to microbuckling, followed by a localized failure mode.

These issues have been addressed for honeycombs by Papka and Kyriakides (1994), who have conducted a series of careful experimental and numerical investigations. They have shown that a consideration of a suitable size of the representative microsection can result in a localized collapse which is energetically preferred to the assumed uniform mode of collapse obtained in the previously mentioned references. Moreover, they carried out full scale numerical calculations, involving finite sized honeycomb specimens, showing deformation propagating from row to row as obtained experimentally.

More recently, taking advantage of the periodic nature of the honeycomb microstructure, Triantafyllidis and Schraad (1998) have performed calculations for capturing the onset of instability under arbitrary macroscopic loading conditions. In their work, they show that the critical mode for an infinite perfectly periodic medium is characterized by a dimensionless wave number ω_c, which is defined as the ratio of the unit cell size to the wavelength of the bifurcation mode shape. The value of this wave number provides an indication as to whether or not a localized failure mode is possible. Moreover, Geymonat et al. (1993) have illustrated the completeness of the Bloch wave representation for capturing the initial instability in finetely strained, rate-independent, perfectly periodic composites, and have proven that, in the case for which $\omega_c \to 0$, the first instability can also be determined from the macroscopic properties of the infinite medium, as the first loss of ellipticity in the incremental homogenized moduli of the material. In addition, the concept of the microfailure and the macrofailure surfaces in macroscopic stress or strain space for finetely strained, periodic media, were introduced by Triantafyllidis and Schnaidt (1993), for the case of biaxially loaded frame models.

In the present study, we are interested in 3D open-cell foams and we try to understand and analyze the major aspects of their mechanical response to macroscopic loadings. We follow the example, set by Pradel (1998), Zhu, Knott, et al. (1997) and several authors, of using periodic beams network with tetrakaidecahedral cells (14 faces defined by 36 edges) as representative model of this class of materials. Given the fact that the onset of bifurcation type instability is the precursor to the ultimate failure mode in these materials, it seems logical to investigate the critical macroscopic stress state, and also to determine the nature of the corresponding critical bifurcation mode. This work is based on the theory of loss of stability in the context of nonconvex homogenization (Geymonat et al., 1993; Müller, 1987; Nguyen, 1995), and on the concept of micro- and macrofailure surfaces introduced by Triantafyllidis and co-workers. It is conducted using ABAQUS in order to provide these surfaces for cellular materials under multiaxial loads. Next, the postbuckling behavior is analyzed for two particular loadings: uniaxial compression ($\underline{\underline{\Sigma}} = \Sigma_{33}\underline{e}_3 \otimes \underline{e}_3$) and uniaxial deformation ($\underline{\underline{E}} = E_{33}\underline{e}_3 \otimes \underline{e}_3$). Finally, the presentation is concluded with a detailed discussion of the results and suggestions for future research.

2. Theoretical background

2.1. Nonlinear homogenization

Consider an hyperelastic solid, with a perfectly periodic microstructure, described by the stored-energy density per unit reference volume $w(\underline{X},\underline{\underline{F}})$. This energy density depends on the position $\underline{X}$ of a material point in the reference configuration and on the local deformation gradient $\underline{\underline{F}}$ defined as $\partial\underline{x}/\partial\underline{X}$ with $\underline{x}$ denoting the position of the material point in the current configuration. It follows that the first Piola–Kirchhoff stress tensor, denoted here by $\underline{\underline{\Sigma}}(\underline{\underline{F}})$, can be easily obtained by differentiation of $w(\underline{X},\underline{\underline{F}})$ with respect to $\underline{\underline{F}}$ ($\underline{\underline{\Sigma}} = \partial w/\partial\underline{\underline{F}}$).

We assume that w is Y-periodic in $\underline{X}$ where $Y = [0,1]^3$ is a unit cell (i.e. $w(\underline{X} + \sum_{i=1,3} n_i\underline{e}_i, \underline{\underline{F}}) = w(\underline{X},\underline{\underline{F}})$ where $n_i|_{i=1,3}$ are arbitrary integers and $\underline{e}_i|_{i=1,3}$ are the basis vectors in the reference configuration). Müller (1987) has shown that under polynomial growth conditions in $\underline{\underline{F}}$, the homogenized (overall) energy density is given by

$$\mathscr{W}^{\hom}(\underline{\underline{F}}) = \inf_{\underline{k}} \left\{ \inf_{\underline{u}^{\mathrm{per}}(\underline{k}Y\text{-periodic})} \left\langle w(\underline{X},\underline{\underline{F}} + \underline{\nabla} \otimes \underline{u}^{\mathrm{per}}) \right\rangle_{\underline{k}Y} \right\}, \tag{1}$$

where $\mathscr{W}^{\hom}$ is the homogenized strain-energy density, $\underline{k} = (k_i)_{i=1,3}$ are positive integers and $\underline{u}^{\mathrm{per}}$ is a $\underline{k}Y$-periodic displacement field with $\underline{k}Y = \prod_{i=1,3}[0,k_i]$ (i.e. $\underline{u}^{\mathrm{per}}(\underline{X} + \sum_{i=1,3} n_i k_i \underline{e}_i) = \underline{u}^{\mathrm{per}}(\underline{X})$ for arbitrary integers $n_i|_{i=1,3}$).

In addition, by $\underline{\nabla} \otimes \underline{v}$ we denote the Lagrangian gradient of a vector $\underline{v}$, i.e. $\partial\underline{v}/\partial\underline{X}$, whereas by $\langle f \rangle_{\Omega}$ we denote the volume-average of f on Ω.

Moreover, Marcellini (1978) has proved that if w is convex, the infinimum in (1) is reached on Y, i.e. for $\underline{k} = (1,1,1)$. So, in the homogenization procedure, when the strain-energy function is not convex, we have to take into account all possible periodic displacement fields on all possible unit cells $\underline{k}Y$.

2.2. Microfailure surface

Let us focus on proportional loading paths, where each path is defined by a fixed macroscopic load orientation $\underline{\underline{\tilde{E}}}$ and an increasing positive parameter λ, as follows:

$$\underline{\underline{F}}(\lambda) = \underline{\underline{E}}(\lambda) + \underline{\underline{I}} = \lambda\underline{\underline{\tilde{E}}} + \underline{\underline{I}}, \tag{2}$$

where $\underline{\underline{I}}$ is the identity tensor.

For instance, for uniaxial deformation along $\underline{e}_3$, $\underline{\underline{\tilde{E}}} = \underline{e}_3 \otimes \underline{e}_3$ and $\lambda = \delta/h$, where δ is the macroscopic displacement and h is the initial height of the structure.

Notice that for $\lambda \ll 1$, linearized elasticity assumptions are valid, and the solution of problem (1) is Y-periodic. It is the trivial solution denoted $\underline{u}^{\mathrm{per}}(\lambda)$ which is defined up to a constant. Then, when λ increases, this solution may lose stability. Let us define the microscopic incremental moduli tensor $\underline{\underline{\underline{\underline{l}}}}(\underline{X},\lambda)$ as

$$l_{ijkl}(\underline{X},\lambda) = \frac{\partial^2 w}{\partial F_{ij}\partial F_{kl}}\left(\underline{X},\underline{\underline{F}}(\lambda) + \underline{\nabla} \otimes \underline{u}^{\mathrm{per}}(\lambda)\right). \tag{3}$$

A critical value $\lambda^{(k)}$ may be defined as the infinimum of λ for which $\underline{k}Y$-periodic instability modes occur, that is

$$\exists \delta\underline{u}(\underline{X}) \neq \text{constant} / \left(l_{ijkl}(\underline{X},\lambda)\delta u(\underline{X})_{k,l}\right)_{,j} = 0, \tag{4}$$

where $f_{,i} = \partial f/\partial X_i$, and in this case $\delta\underline{u}(\underline{X}) = \delta\underline{u}^{\mathrm{per}}(\underline{X})$ is $\underline{k}Y$-periodic.

The critical value λ_c is then defined as the infinimum of $\lambda^{(\underline{k})}$ on all possible periodic unit cells $\underline{k}Y$. This critical load pararmeter λ_c corresponds to the first instability in the infinite periodic model. To the authors' knowledge, this approach has been first used by Abdelmoula et al. (1994) and will be used in the present study.

Moreover, an alternative approach consists in considering Bloch wave modes with nonperiodic displacement fields defined on the unit cell Y by (Triantafyllidis and Bardenhagen, 1996)

$$\delta\underline{u}(\underline{X}) = \delta\underline{u}^{\mathrm{per}}(\underline{X})\mathrm{e}^{i\underline{\omega}\cdot\underline{X}}, \tag{5}$$

where $\delta\underline{u}^{\mathrm{per}}$ is an Y-periodic function of $\underline{X}$ and $\underline{\omega} = (\omega_i)|_{i=1,3} \in [0, 2\pi[^3$ are dimensionless wave numbers of the corresponding bifurcation eigenmode along the $(X_i)|_{i=1,3}$ directions respectively.

For fixed $\underline{\omega}$, let $\lambda_m(\underline{\omega})$ denotes the infinimum value of λ for which Eq. (4) holds with Bloch waves.

Geymonat et al. (1993) have demonstrated that the minimum value of $\lambda_m(\underline{\omega})$ over all wave numbers vectors (i.e. for $0 \leqslant \omega_i|_{i=1,3} < 2\pi$) is equal to the critical load parameter λ_c already introduced. This means that Bloch waves analysis is equivalent to arbitrary periodic waves analysis. Both methods lead to the termed microfailure surface and λ_c will be denoted by $\lambda_c^{\mathrm{micro}}$.

2.3. Macrofailure surface

In the Bloch waves approach, one of the important characteristics of the critical load parameter $\lambda_m(\underline{\omega})$ (see Schraad and Triantafyllidis (1997)) concerns the presence of a singularity at the origin of the dimensionless wave numbers domain (i.e. at $\underline{\omega} = (0, 0, 0)$). As the wave numbers are defined as the ratio of the unit cell size dimensions h_i to the wavelengths L_i of the bifurcation mode shape (i.e. $\omega_i = 2\pi h_i/L_i$), two different types of bifurcation eigenmodes are mapped in the neighborhood of the origin

- $\underline{\omega} = 0$ leads to Y-periodic modes (i.e. $\delta\underline{u}(\underline{x}) = \delta\underline{u}^{\mathrm{per}}(\underline{x})$) as in each direction their wavelengths commensurate with the unit cell size.
- $\underline{\omega} \to 0$ leads to long wavelength modes, much larger than the unit cell size (i.e. $L_i \gg h_i$).

Then, as the critical load for a long wavelength mode does not coincide, in general, with the critical load of an Y-periodic mode, the critical load parameter surface $\lambda_m(\underline{\omega})$ is singular at the origin.

Hence, two different situations are distinguished in the Bloch waves approach. If the critical load λ_c is attained for some finite $\underline{\omega}_c$, the onset of failure is termed "local", whereas if λ_c is obtained as $\underline{\omega}_c$ tends to zero (i.e. $\underline{\omega}_c \to 0$), the onset of failure is termed "global". For the latter case, as the failure mode depends on the overall properties of the medium at the loading state in question, according to Schraad and Triantafyllidis (1997), the critical load for this case can be found by investigating the macroscopic (homogenized) properties of the model.

As a result, a new failure surface is defined as the first loss of ellipticity of the macroscopic incremental moduli tensor $\underline{\underline{\underline{\underline{L}}}}^{\mathrm{hom}}(\lambda)$, obtained by homogenization of the Y-periodic microscopic moduli tensor $\underline{\underline{\underline{\underline{l}}}}(\underline{X}, \lambda)$. More specifically, the macroscopic critical load, denoted by $\lambda_c^{\mathrm{macro}}$, is defined as the minimum value of the load parameter λ along a given loading path for which there exists a unit vector $\underline{n}$ such that the rank-two tensor $\underline{n} \cdot \underline{\underline{\underline{\underline{L}}}}^{\mathrm{hom}}(\lambda) \cdot \underline{n}$ (termed the "acoustic tensor") loses positive definiteness. The resulting failure surface, which is defined in macroscopic strain space, is termed macrofailure surface. Notice that, the macroscopic critical load is always greater than or equal to the microscopic critical load (i.e. $\lambda_c^{\mathrm{macro}} \geqslant \lambda_c^{\mathrm{micro}}$), with the equality achieved when, in the microscopic analysis, the minimum of $\lambda_m(\underline{\omega})$ is obtained for $\underline{\omega} \to 0$. This is logical as $\underline{\omega} \to 0$ is a particular case of the Bloch waves approach which consists in performing a minimization over all possible $\underline{\omega}$. Hence, the macrofailure surface for an infinite medium with perfectly periodic microstructure provides an upper bound for the corresponding microfailure surface.

It has been also demonstrated that when $\lambda_c^{macro} = \lambda_c^{micro}$, this critical value is also the infinimum of λ for which Eq. (4) holds for instability modes of the following form:

$$\delta\underline{u}(\underline{X}) = \delta\underline{u}^{per}(\underline{X}) + (\underline{m} \otimes \underline{n}) \cdot \underline{X}, \tag{6}$$

where $\delta\underline{u}^{per}$ is Y-periodic and $\underline{m}$ and $\underline{n}$ are unit vectors. In addition, the post-bifurcation failure mode is shown to develop into a macroscopically localized mode of failure of the shear band or kink band type, which is characterized by $\underline{n}$ and $\underline{m}$: $\underline{n}$ is the normal vector to the band plane and $\underline{m}$ gives the displacement direction of the band.

2.4. Mixed failure surface

In their study on honeycombs, Triantafyllidis and Schraad (1998) have obtained for their particular case that λ_c^{micro} is achieved at the origin of the wave numbers domain, i.e. either for Y-periodic displacements variations ($\underline{\omega} = 0$) or for long wavelength displacements variations ($\underline{\omega} \to 0$).

Our purpose is then to develop a procedure which takes into account both Y-periodic and long wavelength displacements variations. To achieve this, we notice that if $\underline{m}$ in (6) is zero, then $\delta\underline{u}$ is Y-periodic. Now, for fixed unit vector $\underline{n}$, let $\lambda^{mixed}(\underline{n})$ be the infinimum of λ for which Eq. (4) holds for instability modes of form:

$$\delta\underline{u}(\underline{X}) = \delta\underline{u}^{per}(\underline{X}) + (\delta\underline{\mathscr{U}} \otimes \underline{n}) \cdot \underline{X}, \tag{7}$$

where $\delta\underline{\mathscr{U}}$ is arbitrary and $\delta\underline{u}^{per}$ is Y-periodic. Then λ_c^{mixed} is defined as the minimum of $\lambda^{mixed}(\underline{n})$ over $\underline{n}$ (i.e. $\lambda_c^{mixed} = \min_{\underline{n}} \lambda^{mixed}(\underline{n})$). The resulting failure surface, which is defined in macroscopic strain space, is termed mixed failure surface. Notice that, the macroscopic critical load is always greater than or equal to the mixed critical load, which is in his turn greater than or equal to the microscopic critical load (i.e. $\lambda_c^{macro} \geqslant \lambda_c^{mixed} \geqslant \lambda_c^{micro}$). Denoting by $\underline{n}_c$ a vector $\underline{n}$ for which $\lambda_c^{mixed} = \lambda^{mixed}(\underline{n}_c)$, the equality $\lambda_c^{mixed} = \lambda_c^{macro}$ is achieved when, in the mixed approach, the $\delta\underline{\mathscr{U}}$ corresponding to $\underline{n}_c$ is not zero.

In the aforementionned work of Triantafyllidis and Schraad (1998), we notice that what we call mixed failure surface coincides with the microfailure surface they obtained. In addition, our numerical study will also show that the mixed failure surface of a tetrakaidecahedral lattice coincides with its microfailure surface (Section 4.4). An interesting theoretical issue is to identify a priori conditions which ensure that these two failure surfaces coincide. Indeed, mixed failure surface gives informations, provided by $\delta\underline{\mathscr{U}}$ and $\underline{n}$, on possible localized macroscopic modes of failure. Moreover, it is easier to compute than both methods: the scheme which uses large representative volumes with $\underline{k}$Y-periodic functions and the scheme with the Bloch wave representation.

3. Application to open-cell foams

3.1. Open-cell foam modeling

The compressive response of 2D and 3D cellular solids has been examined experimentally by Gibson and Ashby (1982), Gibson et al. (1982), Maiti et al. (1984), Papka and Kyriakides (1998) and several authors. These materials deform considerably at low forces. Their load–displacement response is characterized by three regimes. First, the material has a relatively high stiffness given by a sharp initial rise to a load maximum. It is often a linear elastic regime. Then, the material has almost zero stiffness and an extended load plateau is observed. It is termed the plateau regime. Finally, the response becomes stiff given by a sharp rise in load again. It is known as the densification regime.

In this investigation open-foams are modeled by a lattice composed of periodic tetrakaidecahedral cells. The finite elements method is used to discretize the lattice into linear elastic beams. Actually, the mechanism-rich behavior in the experiments results from a complex interaction between nonlinearities of geometry, material and contact present in the problem. We will focus on geometrical nonlinearities. The cell edges are modeled by two-noded, linear Timoshenko (shear deformable) beam elements, which are based on nonlinear kinematics allowing for large axial strains (ABAQUS B31 element). The number of elements used in the calculations has been determined from convergence tests and is given in the Appendix. The considered isotropic linear elastic behavior of the solid material is given by the stored-energy density:

$$w(\underline{\underline{F}}) = \frac{1}{2}\underline{\underline{e}}^{\mathrm{T}} : \underline{\underline{\underline{c}}} : \underline{\underline{e}}, \tag{8}$$

where $\underline{\underline{e}} = 1/2(\underline{\underline{F}}^{\mathrm{T}}\underline{\underline{F}} - \underline{\underline{I}})$ is the Lagrangian strain tensor and

$$c_{ijkl} = \frac{E_{\mathrm{s}}}{2(1+\nu_{\mathrm{s}})}(\delta_{ik}\delta_{jl} + \delta_{il}\delta_{jk}) + \frac{\nu_{\mathrm{s}}E_{\mathrm{s}}}{(1+\nu_{\mathrm{s}})(1-2\nu_{\mathrm{s}})}\delta_{ij}\delta_{kl}, \tag{9}$$

where E_{s} is the solid Young's modulus, ν_{s} is the solid Poisson's ratio and δ_{ij} is the Krönecker symbol.

Methods for evaluating the linear elastic properties of materials with microstructure are well established and will not be discussed here (for the elastic properties of honeycomb see, for example, Gibson and Ashby (1982), Pradel and Sab (1998) and Warren and Kraynik (1987); for problems with open-cell foams with periodic tetrakaidecahedral cells see, for instance, Pradel (1998), Zhu, Knott, et al. (1997) and Warren and Kraynik (1988)]. For a tetrakaidecahedral lattice of Euler–Bernoulli beams, in small strain analysis, the behavior is shown to be fully described by three independent elastic coefficients: the homogenized Young's modulus E_{hom}, the homogenized Poisson's ratio ν_{hom} and the homogenized shear modulus G_{hom}. They are respectively given by

$$E_{\mathrm{hom}} = 6\sqrt{2}\frac{SI_1E_{\mathrm{s}}}{l^2(12I_1 + l^2S)}, \tag{10}$$

$$\nu_{\mathrm{hom}} = -\frac{1}{2}\frac{12I_1 - l^2S}{12I_1 + l^2S} \tag{11}$$

and

$$G_{\mathrm{hom}} = \frac{3\sqrt{2}SI_2E_{\mathrm{s}}\left(I_2 + \frac{G_{\mathrm{s}}}{E_{\mathrm{s}}}I_{\mathrm{t}} + 4I_1\right)}{l^2\left(12I_2^2 + 48I_2I_1 + 12I_2\frac{G_{\mathrm{s}}}{E_{\mathrm{s}}}I_{\mathrm{t}} + l^2\frac{G_{\mathrm{s}}}{E_{\mathrm{s}}}I_{\mathrm{t}}S + 4l^2SI_2 + 4l^2SI_1\right)}, \tag{12}$$

where S is the beam's area, l is the beam's length, I_1 is the moment of inertia along the first beam's principal axis, I_2 is the moment of inertia along the second beam's principal axis, I_{t} is the torsion moment of inertia, and $G_{\mathrm{s}} = E_{\mathrm{s}}/2(1+\nu_{\mathrm{s}})$ is the solid shear modulus.

Furthermore, in the termed uniaxial deformation explained below, we define a modulus $E_{\mathrm{œd}}$ as the ratio of the stress by the strain along the loading axis. This modulus is given analytically by

$$E_{\mathrm{œd}} = \frac{E_{\mathrm{hom}}}{\frac{2\nu_{\mathrm{hom}}^2}{\nu_{\mathrm{hom}}-1} + 1}. \tag{13}$$

As explained in Section 2.2, for proportional loading paths (2), the small strain solution of problem (1), denoted by $\underline{u}^{\mathrm{per}}(\lambda)$, is Y-periodic. However, as λ increases, the solution may lose stability. In order to perform the stability analysis, we follow Nguyen (1995) by introducing two assumptions. The first one, (A1), is termed small pre-deformations assumption: $\underline{u}^{\mathrm{per}}(\lambda)$ is "small" and linear in λ (i.e. $\underline{u}^{\mathrm{per}}(\lambda) \simeq \lambda\underline{\tilde{u}}^{\mathrm{per}}$,

where $\tilde{\underline{u}}^{\text{per}}$ denotes the solution for $\lambda = 1$ in linear elasticity). The second one, (A2), consists in neglecting the second order terms in λ in the second variations of the unit cell energy.

Now, if $\lambda_{\text{critical}}$ is the critical value of λ for a given set of variations, we will get

$$\lambda_{\text{critical}} = \min_{\delta\underline{u}} -\frac{\int_\Omega \delta\underline{\underline{\epsilon}} : \underline{\underline{\underline{\underline{c}}}} : \delta\underline{\underline{\epsilon}} \mathrm{d}\Omega}{\int_\Omega \tilde{\underline{\underline{\sigma}}} : ((\underline{\nabla} \otimes \delta\underline{u})^{\mathrm{T}} \cdot \underline{\nabla} \otimes \delta\underline{u}) \mathrm{d}\Omega}, \tag{14}$$

where $\delta\underline{\underline{\epsilon}} = 1/2\left[(\underline{\nabla} \otimes \delta\underline{u}) + (\underline{\nabla} \otimes \delta\underline{u})^{\mathrm{T}}\right]$ denotes the linearized Lagrangian strain tensor, and $\tilde{\underline{\underline{\sigma}}}$ is the stress tensor field corresponding to $\tilde{\underline{u}}^{\text{per}}$.

We shall perform the stability analysis of the following proportional loading paths:

$$\underline{\underline{F}}(\lambda) = \lambda(\alpha_1 \underline{e}_1 \otimes \underline{e}_1 + \alpha_2 \underline{e}_2 \otimes \underline{e}_2 + \underline{e}_3 \otimes \underline{e}_3) + \underline{\underline{I}}, \tag{15}$$

where $\underline{e}_i|_{i=1,3}$ are the principal axis and $\alpha_i|_{i=1,2}$ are the varying parameters. These paths correspond to

$$\tilde{\underline{\underline{E}}} = \alpha_1 \underline{e}_1 \otimes \underline{e}_1 + \alpha_2 \underline{e}_2 \otimes \underline{e}_2 + \underline{e}_3 \otimes \underline{e}_3. \tag{16}$$

Therefore, the loadings are macroscopic strains depending on the increasing parameter $\lambda = E_{33}$. They are applied to the infinite lattice through periodicity conditions on the nodes located at the boundary of the unit cell (Section 3.3).

The failure surfaces are obtained by varying α_1 and α_2 in (15) and they are mapped in principal macroscopic stress space. Actually, for given α_1 and α_2, we compute the first positive eigenvalue λ_c^+ and the first negative eigenvalue λ_c^-. The latter one corresponds to the first positive eigenvalue of the loading path

$$\underline{\underline{F}}(\lambda) = -\lambda(\alpha_1 \underline{e}_1 \otimes \underline{e}_1 + \alpha_2 \underline{e}_2 \otimes \underline{e}_2 + \underline{e}_3 \otimes \underline{e}_3) + \underline{\underline{I}}.$$

In order to compute these surfaces, the approaches already described in Sections 2.2 and 2.4 are used: the periodic waves approach (i.e. for given loading paths, we consider periodic displacements variations on bigger and bigger size of unit cells), and the mixed waves approach (i.e. for given loading paths, we consider nonperiodic displacements (7) variations on a minimum size unit cell).

Moreover, in order to perform nonlinear analyses, we will focus on two particular loadings:

1. Uniaxial deformation defined by a macroscopic deformation gradient tensor $\underline{\underline{F}}$ where $\alpha_1 = \alpha_2 = 0$ in (15), i.e. $\underline{\underline{E}} = E_{33} \underline{e}_3 \otimes \underline{e}_3$. It corresponds to a compression test with restrained horizontal displacements.
2. Uniaxial compression defined by a macroscopic Piola–Kirchhoff stress tensor $\underline{\underline{\Sigma}} = \Sigma_{33} \underline{e}_3 \otimes \underline{e}_3$. We will provide in Section 3.3.2 a detailed description of the boundary conditions we use in this case.

3.2. Unit cells geometry

A unit cell of the open-cell foam with tetrakaidecahedral cells is chosen such as, when compressed, it yields results representative of those which take place in large multicell foam specimen. A minimum unit cell, termed $C_{\min}$, has been identified by Pradel (1998). Denoting by "a" the height of the unit tetrakaidecahedral cell, $C_{\min}$ fills the space limited by a (a,a,a/2) parallelepiped, and is equivalent, in volume, to one tetrakaidecahedron. This unit cell consists in 12 geometrical nodes which belong to six node classes induced by the lattice periodicity and which are joined by 12 edges, as shown in Fig. 1.

However, in order to be able to simulate some nonsymmetric deformation modes of less energy than the symmetric modes used by Zhu, Mills, et al. (1997) and Pradel (1998), we followed the approach presented by Papka and Kyriakides (1994) for 2D honeycombs, and we extended it to the lattice under study. This led us to a periodic unit cell, termed CB, presented in Fig. 2 and consisting of a central unit tetrakaidecahedron surrounded by 10 half tetrakaidecahedra laterally and two half tetrakaidecahedra on the top and on the

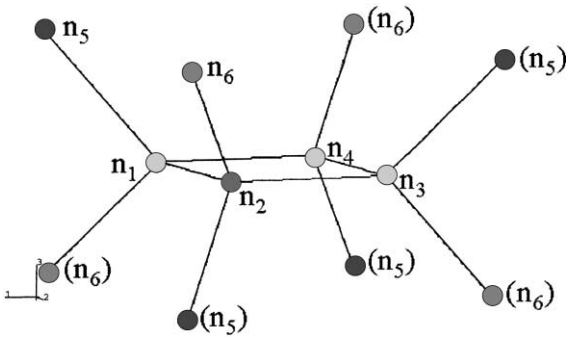

Fig. 1. A minimum periodic unit cell: $C_{\min}$.

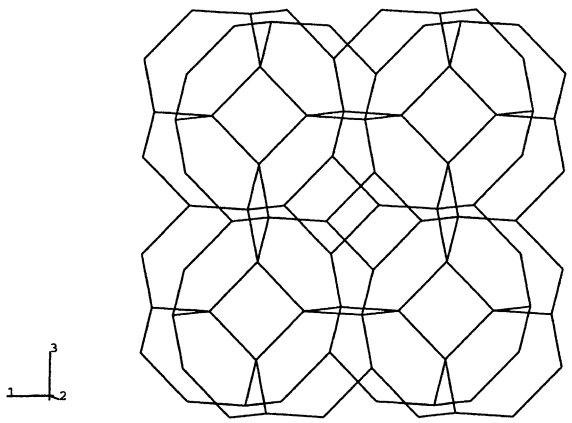

Fig. 2. A parallelipipedic unit cell CB.

bottom. This new unit cell is included in a (2a,a,2a) parallelepiped and is equivalent in volume to eight tetrakaidecahedra.

As the uniaxial loadings in the geometrically nonlinear analysis are applied along the $\underline{e}_3$ axis, we superposed on the top and on the bottom of the CB two more CB. This resulted in the termed CB3, presented in Fig. 3(a). This unit cell is included in a (2a,a,6a) parallelepiped and is then equivalent to 24 tetrakaidecahedra.

Then, we added two more CB on the top and on the bottom of the CB3, obtaining the termed CB5, presented in Fig. 3(b). This unit cell is included in a (2a,a,10a) parallelepiped and is then equivalent to 40 tetrakaidecahedra.

Finally, we constructed the unit cell termed CB333 and presented in Fig. 3(c). This unit cell is included in a (6a,6a,6a) parallelepiped, and is equivalent to 432 tetrakaidecahedra. This resulted in 32160 nodes and 22464 elements for the discretized CB333, whereas the minimum cell $C_{\min}$ has only 91 nodes and 48 elements (see Appendix).

3.3. Periodicity conditions

In order for a unit cell to be representative of an infinite periodic structure, periodicity conditions have to be applied to all the nodes which are located on the boundary faces of this unit cell. Notice that for CB,

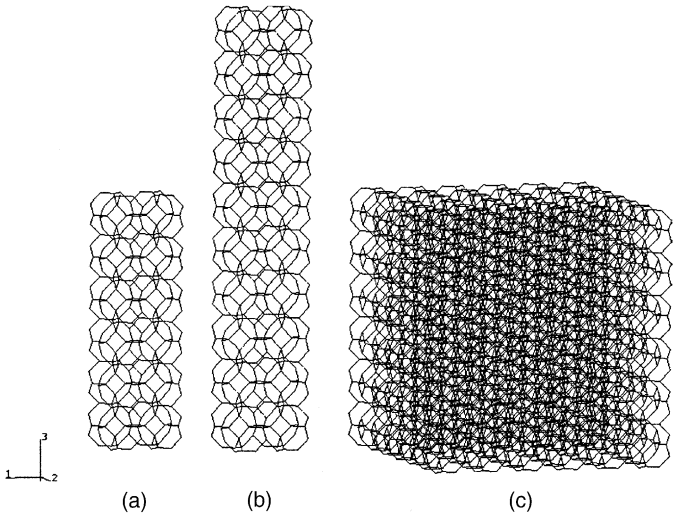

Fig. 3. Multiple parallelipipedic unit cells: (a) CB3, (b) CB5, (c) CB333.

CB3, CB5 and CB333, the matching rule for the nodes is standard: the matched nodes are the couple of nodes which are on opposite boundary faces. However, for $C_{\min}$, the matched nodes are those numbered n_5 and those numbered n_6 in Fig. 1.

We denote by

- C the considered unit cell;
- ∂C^{i+} and ∂C^{i-} the boundary faces of C respectively normal to $\underline{e}_i$ and $-\underline{e}_i$;
- $\underline{X}^{i+}$ and $\underline{X}^{i-}$ the position vector in the reference configuration of matched nodes respectively on ∂C^{i+} and ∂C^{i-};
- $\underline{U}^{i+}$ and $\underline{U}^{i-}$ the displacements of these matched nodes;
- $\underline{\phi}^{i+}$ and $\underline{\phi}^{i-}$ their corresponding rotations.

Notice that, except for $C_{\min}$ we have, $X_j^{i+} = X_j^{i-}$ for $j \neq i$.

3.3.1. Prescribed strain loadings

For proportional loading paths with prescribed strains, i.e. with given α_1, α_2 in (15), the periodicity conditions are as follows:

$$\begin{cases} \underline{U}^{i+} - \underline{U}^{i-} = \underline{\underline{E}}(\lambda) \cdot (\underline{X}^{i+} - \underline{X}^{i-}) \\ \underline{\phi}^{i+} - \underline{\phi}^{i-} = 0 \end{cases}. \tag{17}$$

For example, in uniaxial deformation along $\underline{e}_3$, $\underline{\underline{E}}(\lambda) = \lambda \underline{e}_3 \otimes \underline{e}_3$. Hence, except for $C_{\min}$, the following symmetry and matching conditions are used:

1. The displacements and rotations of nodes $\underline{X}^{1+}$ and nodes $\underline{X}^{2+}$ are matched with the same degrees of freedom of nodes $\underline{X}^{1-}$ and nodes $\underline{X}^{2-}$, respectively.
2. The horizontal displacements and rotations of nodes $\underline{X}^{3+}$ are matched with those of nodes $\underline{X}^{3-}$.
3. The deformation of the unit cell is performed by constraining the difference between the vertical displacements of nodes $\underline{X}^{3+}$ and nodes $\underline{X}^{3-}$ to be equal to $\delta = \lambda h$, where h is the initial height of the unit cell.

4. Also, to avoid arbitrary rigid motions, the horizontal displacements u_1, u_2 and the rotation φ_3 of one choosen node in the unit cell is prescribed to be zero.

3.3.2. Uniaxial compression

We recall that the first Piola–Kirchhoff stress tensor is defined by:

$$\underline{\underline{\Sigma}}(\underline{\underline{F}}) = \frac{\partial \mathscr{W}^{\hom}(\underline{\underline{F}})}{\partial \underline{\underline{F}}}. \tag{18}$$

In order to prescribe uniaxial compression along $\underline{e}_3$, we apply periodicity conditions of the form (17) where E_{33} is prescribed and $E_{ij}|_{(i,j)\neq(3,3)}$ are unknown degrees of freedom. Indeed, the stationarity of the energy deformation of the unit cell will lead to

$$\frac{\partial \mathscr{W}^{\hom}}{\partial E_{ij}} = \frac{\partial \mathscr{W}^{\hom}}{\partial F_{ij}} = \Sigma_{ij} = 0 \quad \text{for } (i,j) \neq (3,3). \tag{19}$$

Thus, we choose reference pair of matched nodes $(\underline{X}^{i+}_{\text{ref}}, \underline{X}^{i-}_{\text{ref}})$ for each pair of boundary faces $(\partial C^{i+}, \partial C^{i-})$. Their displacements and rotations are respectively denoted by $(\underline{U}^{i+}_{\text{ref}}, \underline{U}^{i-}_{\text{ref}})$ and $(\underline{\phi}^{i+}_{\text{ref}}, \underline{\phi}^{i-}_{\text{ref}})$. The displacements of the reference pairs $(\underline{X}^{i+}_{\text{ref}}, \underline{X}^{i-}_{\text{ref}})$ are matched with those of the other pairs of nodes $(\underline{X}^{i+}, \underline{X}^{i-})$. In addition, the rotations of $(\underline{X}^{i+}, \underline{X}^{i-})$ are matched. This leads to the following periodicity conditions:

1. Reference pairs of nodes,

$$\underline{\phi}^{i+}_{\text{ref}} - \underline{\phi}^{i-}_{\text{ref}} = 0;$$

2. Matched nodes at $(\partial C^{1+}, \partial C^{1-})$,

$$\begin{cases} (\underline{U}^{1+} - \underline{U}^{1-}) - (\underline{U}^{1+}_{\text{ref}} - \underline{U}^{1-}_{\text{ref}}) = 0 \\ \underline{\phi}^{1+} - \underline{\phi}^{1-} = 0 \end{cases};$$

3. Matched nodes at $(\partial C^{2+}, \partial C^{2-})$,

$$\begin{cases} (\underline{U}^{2+} - \underline{U}^{2-}) - (\underline{U}^{2+}_{\text{ref}} - \underline{U}^{2-}_{\text{ref}}) = 0 \\ \underline{\phi}^{2+} - \underline{\phi}^{2-} = 0 \end{cases};$$

4. Matched nodes at $(\partial C^{3+}, \partial C^{3-})$,

$$\begin{cases} (U^{3+}_1 - U^{3-}_1) - (U^{3+}_{1\text{ref}} - U^{3-}_{1\text{ref}}) = 0 \\ (U^{3+}_2 - U^{3-}_2) - (U^{3+}_{2\text{ref}} - U^{3-}_{2\text{ref}}) = 0 \\ U^{3+}_3 - U^{3-}_3 = \lambda h \\ \underline{\phi}^{3+} - \underline{\phi}^{3-} = 0 \end{cases}.$$

3.4. Numerical procedures

3.4.1. Linear and nonlinear analyses

Having defined the geometric model, the loadings paths and the periodicity conditions, we first perform a classical linear analysis for both loadings: uniaxial compression and uniaxial deformation, on unit cells of increasing size ($C_{\min}$, CB, CB3 and CB5).

In addition, a geometrically nonlinear analysis for both loadings is performed and compared to Zhu, Mills, et al. (1997) analytical results.

3.4.2. Buckling analyses

We define a failure surface in macroscopic stress space by the onset of the first buckling-type instability encountered along proportional load paths. In order to determine this surface, buckling analysis is performed for different loadings (by varying α_1 and α_2) through two different procedures leading to two failure surfaces:

Microfailure surface: We consider loading paths of the form (15). For fixed α_1, α_2 and $\underline{k}$, we perform standard buckling analyses on unit cells $\underline{k}Y$ (by using the BUCKLE module of ABAQUS) to determine $\lambda^{(\underline{k})}$ already defined. Notice that as the loadings are applied through periodicity conditions (17), this results in $\underline{k}Y$-periodic displacements and rotations variations ($\delta\underline{U}^{i+} - \delta\underline{U}^{i-} = 0$ and $\delta\underline{\phi}^{i+} - \delta\underline{\phi}^{i-} = 0$). Failure surfaces are obtained by varying α_1 and α_2 for each unit cell (from $C_{\min}$ to CB333). The aforementioned microfailure surface is the one for which the critical loads are minimum.

Mixed failure surface: In this approach, we consider the same loading paths of the form (15). In order to determine $\lambda^{\text{mixed}}(\underline{n})$ for fixed α_1, α_2 and unit vector $\underline{n}$, we introduce the following boundary conditions on $C_{\min}$:

$$\begin{cases} \underline{U}^{i+} - \underline{U}^{i-} = \lambda\underline{\underline{\tilde{E}}}(\alpha_1,\alpha_2)\cdot(\underline{X}^{i+} - \underline{X}^{i-}) + (\underline{n}\cdot(\underline{X}^{i+} - \underline{X}^{i-}))\underline{\mathscr{U}} \\ \underline{\phi}^{i+} - \underline{\phi}^{i-} = 0 \end{cases}, \tag{20}$$

where $\underline{\mathscr{U}}$ is the unknown displacement vector of a termed virtual node. Then, the boundary conditions variations are

$$\begin{cases} \delta\underline{U}^{i+} - \delta\underline{U}^{i-} = (\underline{n}\cdot(\underline{X}^{i+} - \underline{X}^{i-}))\delta\underline{\mathscr{U}} \\ \delta\underline{\phi}^{i+} - \delta\underline{\phi}^{i-} = 0 \end{cases}, \tag{21}$$

which coincides with (7).

The idea is to apply a force, denoted by $\underline{R}$, on the virtual node such that the resulting $\underline{\mathscr{U}}$ is zero. In this way, the application of (20) and $\underline{R}$ leads to the same loading defined by (17), whereas the variations are of the form (7). In order to compute $\underline{R}$, we prescribe the virtual node displacements to zero and we identify the reaction force $\underline{R}$. Actually, for fixed α_1 and α_2 it is easy to see that $\underline{R}$ depends linearly on $\underline{n}$ and λ: $\underline{R} = \lambda\underline{\underline{D}}\cdot\underline{n}$. Therefore, the second-order tensor $\underline{\underline{D}}$ can be computed considering three basis vectors ($\underline{n}_1 = (1,0,0)$, $\underline{n}_2 = (0,1,0)$ and $\underline{n}_3 = (0,0,1)$), with $\lambda = 1$. Once $\underline{\underline{D}}$ determined for given α_1 and α_2, we perform buckling analysis for several unit vectors $\underline{n}$. Then λ_c^{mixed} is the minimum of $\lambda^{\text{mixed}}(\underline{n})$.

3.4.3. Postbuckling analysis

The next issue to be addressed concerns the foam behavior under finite strains. As the characteristic plateau regime of the foam's behavior has not been exhibited when (Zhu, Mills, et al., 1997) have performed a classical nonlinear analysis, we will conduct an elastic postbuckling analysis by introducing a geometrical imperfection which has the form of the first buckling mode.

4. Results and discussion

The relative density of interest in the open-cell foams we study is in a range of 0.02–0.1. The results presented below, from Sections 4.1–4.6, concerns a tetrakaidecahedral lattice of Timoshenko beams having a relative density of 0.06. All the results are represented in terms of normalized stress by the solid Young's modulus E_s multiplied by the square of the relative density $R = \rho_f/\rho_s$, where ρ_f and ρ_s are respectively the foam density and the solid density ($\underline{\underline{\Sigma}}^* = \underline{\underline{\Sigma}}/(E_s R^2)$).

4.1. Small strain analysis

In a small strain elastic analysis on the minimum unit cell $C_{\min}$, we recover the already known analytical results (Pradel, 1998; Zhu, Knott, et al., 1997). Actually, the Young's modulus (uniaxial compression) and $E_{\text{œd}}$ (uniaxial deformation) are identical for all the considered unit cells (maximum relative error of 0.07%). This is expected since the energy is convex in small strain analysis. On the other hand, the maximum relative error between the numerical analysis performed on $C_{\min}$ and the analytical ones (from the expressions (10) and (13) respectively) is 1.4%. This is due to Euler–Bernoulli beam assumptions in the analytical expressions. We have also checked that the macroscopic Poisson's ratio is in good agreement with the analytical one given by (11).

4.2. Geometrically nonlinear analysis with symmetrical modes

In a geometrically nonlinear analysis performed on $C_{\min}$, similar to the one performed analytically by Zhu, Mills, et al. (1997) we checked that the initial slope is equal to the one obtained by the corresponding small strain analysis. We also checked that the results are the same when increasing the unit cell size from $C_{\min}$ to CB and CB3. Our geometrically nonlinear numerical analysis, as well as Zhu, Mills, et al. (1997) analysis, does not exhibit the plateau regime (see the curves denoted by "Nonlinear" in Figs. 4 and 5).

4.3. Microfailure surface

The critical load values converge when performing the periodic waves approach on unit cells with increasing size, from $C_{\min}$ to CB333 (Figs. 6 and 7). Notice that, even though the minimum periodic unit cell $C_{\min}$ is enough to study the elastic properties of the lattice in a small strain analysis, its buckling exhibits symmetrical modes of higher energy than the nonsymmetrical modes given by a larger unit cell. The unit cell CB is shown to be representative for some loadings, such as the uniaxial deformation. However, it is not

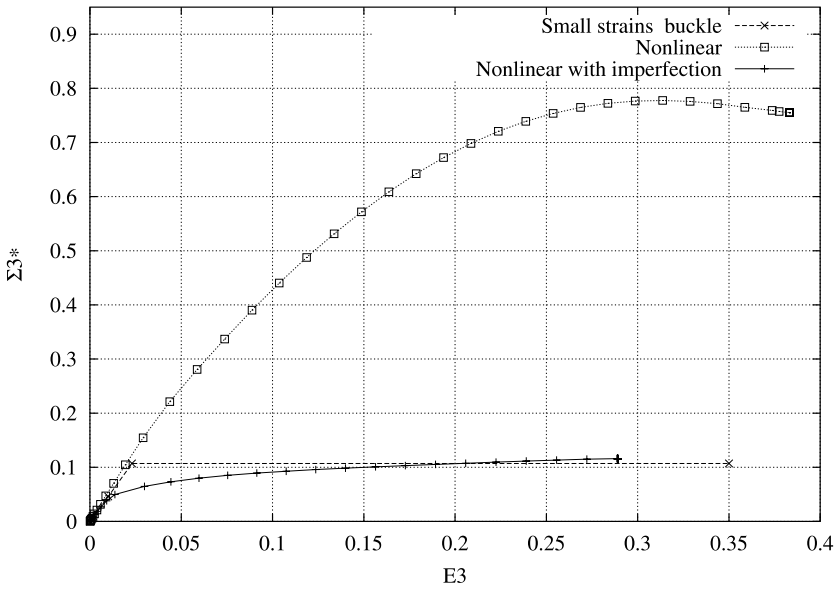

Fig. 4. Uniaxial deformation stress–strain curves.

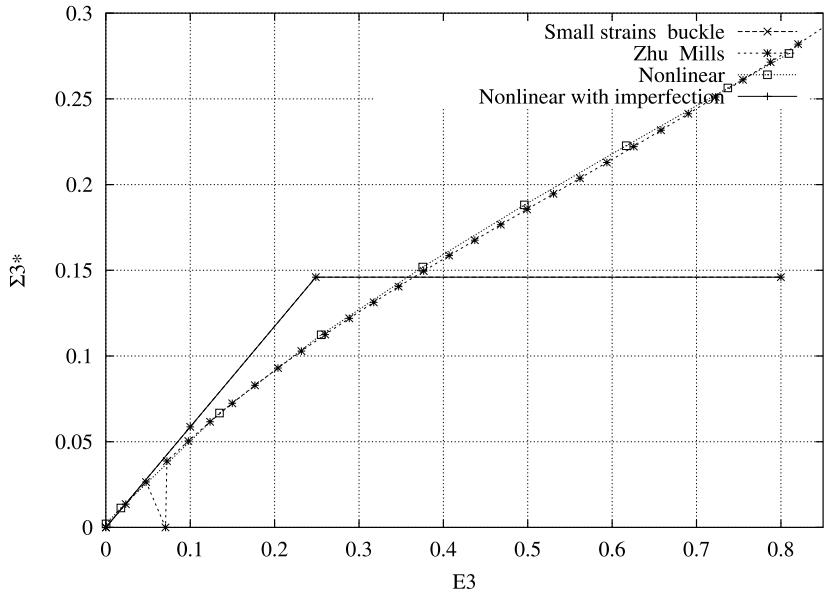

Fig. 5. Uniaxial compression stress–strain curves.

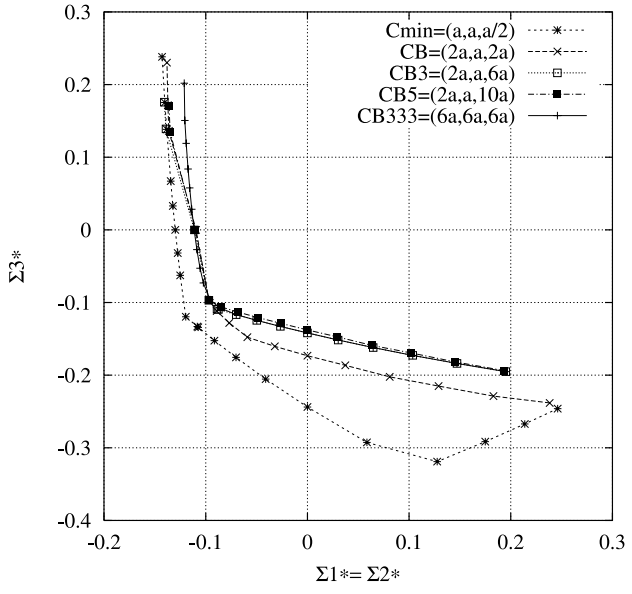

Fig. 6. Convergence of the failure surfaces obtained by the periodic waves approach performed on different unit cell sizes: $\Sigma_1 = \Sigma_2$ plane.

representative for uniaxial compression. Actually, the critical loads obtained for uniaxial compression on CB3 and CB5 are the same. The minimum size representative unit cell is thus shown to be load dependent. Increasing the height of the unit cell in the direction of the major stress, our numerical results have shown

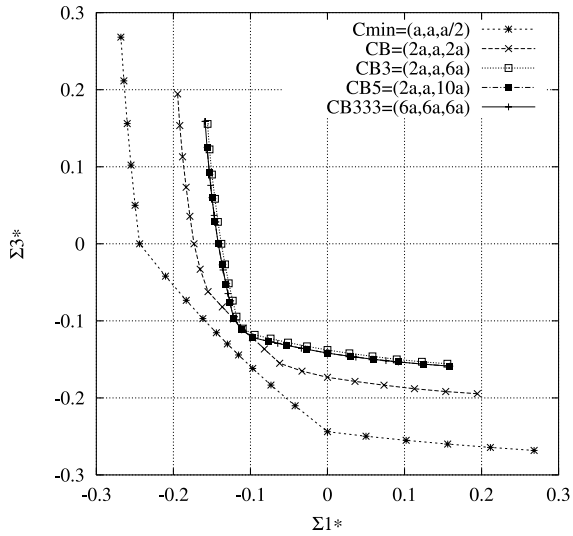

Fig. 7. Convergence of the failure surfaces obtained by the periodic waves approach performed on different unit cell sizes: $\Sigma_2 = 0$ plane.

that a height of 6a is sufficient to reach the convergence. In addition, we checked that by doubling horizontally the size of CB and CB3 (resulting in (2a, 2a, 2a) and (2a, 2a, 6a) unit cells), the results are the same.

Moreover, for uniaxial deformation, the eigenmodes of CB and CB3 are the same (Figs. 8 and 9): it is a local buckling mode. Whereas, for uniaxial compression, the eigenmodes of CB and CB3 are different (Figs. 10 and 11). The eigenmode of CB5 (Fig. 12) has the form of that of CB3 but with a longer wavelength: it is a global buckling mode.

Finally, the unit cell termed CB333 seems to be representative for all the considered loading paths. The resulting failure surface is the numerical approximation of the microfailure surface. It is mapped within two planes: the $\Sigma_1 = \Sigma_2$ and the $\Sigma_2 = 0$ planes, where Σ_i denote the principal macroscopic stresses. Notice that, due to symmetry considerations, the last plane is equivalent to the $\Sigma_1 = 0$ plane. To map this surface in the $\Sigma_1 = \Sigma_2$ plane, 18 numerical calculations per unit cell had been performed. As, in general, each calculation gives a positive and a negative eigenvalue, the total number of mapped critical loads is 29. Whereas the

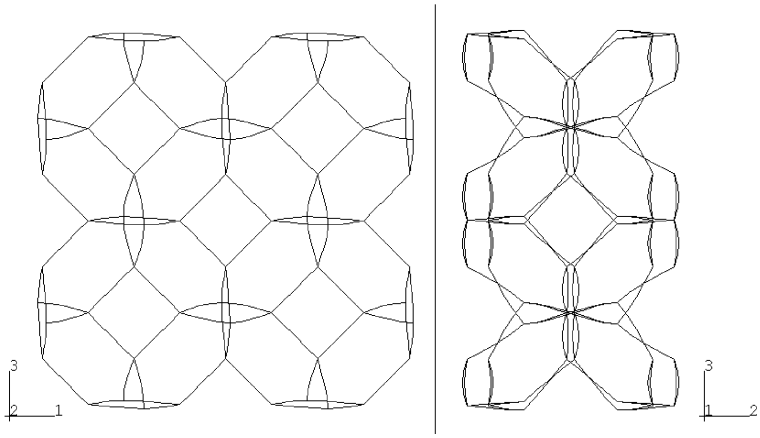

Fig. 8. Buckling mode of CB for uniaxial deformation.

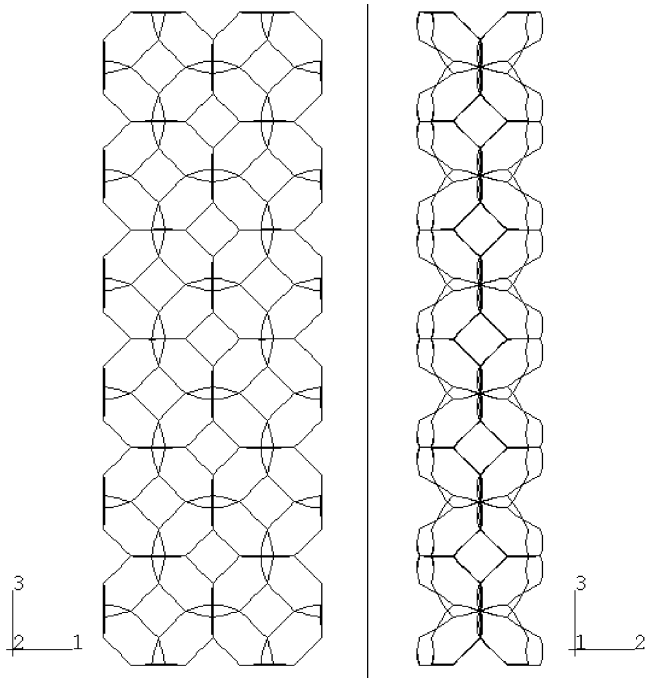

Fig. 9. Buckling mode of CB3 for uniaxial deformation.

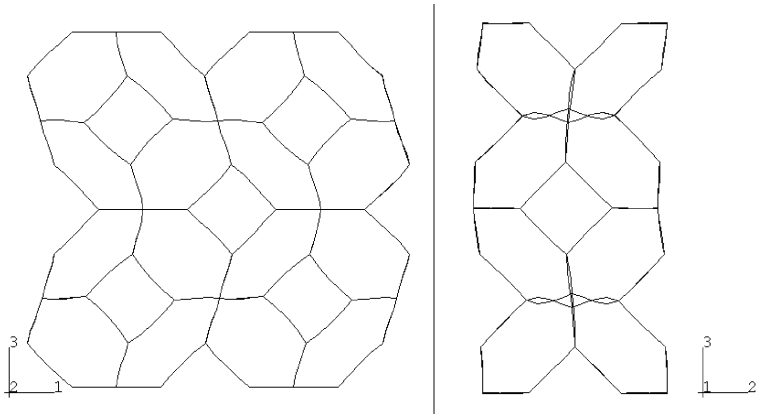

Fig. 10. Buckling mode of CB for uniaxial compression.

number of calculations performed to map the $\Sigma_2 = 0$ plane is 16 and, due to symmetry conditions, the total number of critical loads mapped is 40.

4.4. Mixed failure surface

The mixed approach, introduced in Section 3.3.2, is performed on the minimum unit cell $C_{\min}$. It is shown in Figs. 13 and 14 that the mixed failure surface coincides with the microfailure surface (CB333) up to a maximum relative error of 3.7%.

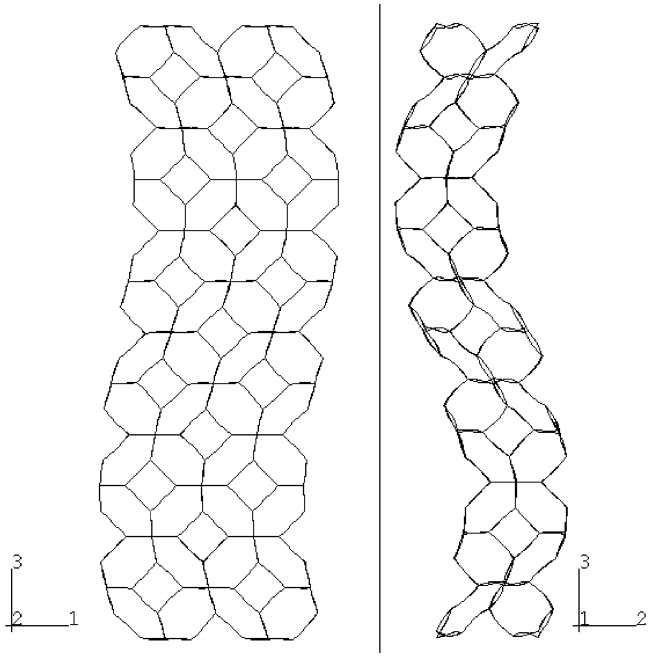

Fig. 11. Buckling mode of CB3 for uniaxial compression.

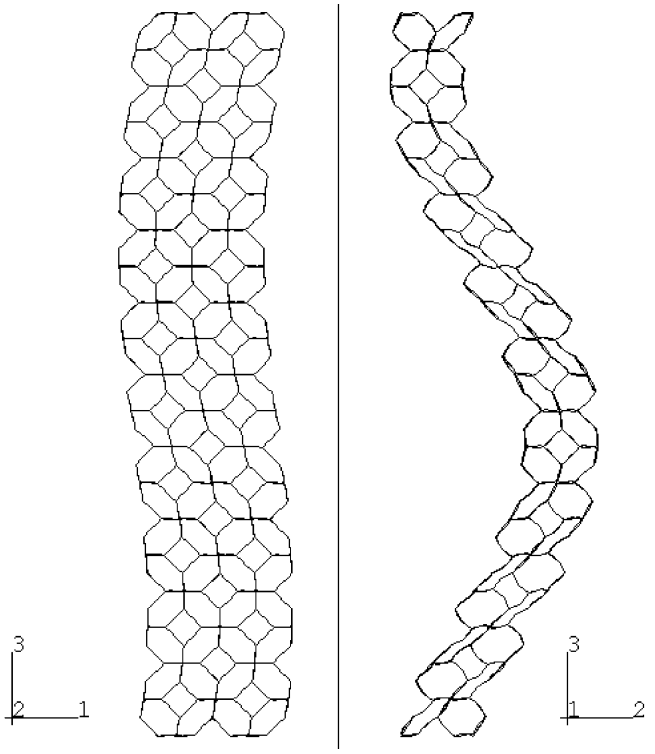

Fig. 12. Buckling mode of CB5 for uniaxial compression.

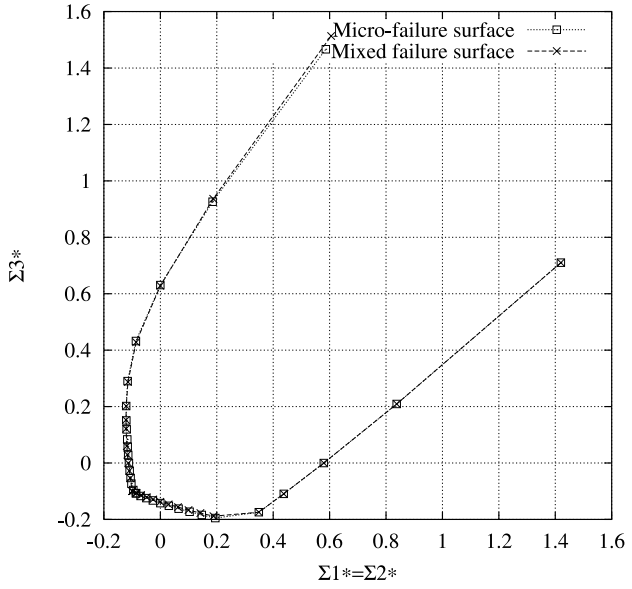

Fig. 13. Micro- and mixed failure surfaces in the $\Sigma_1 = \Sigma_2$ plane.

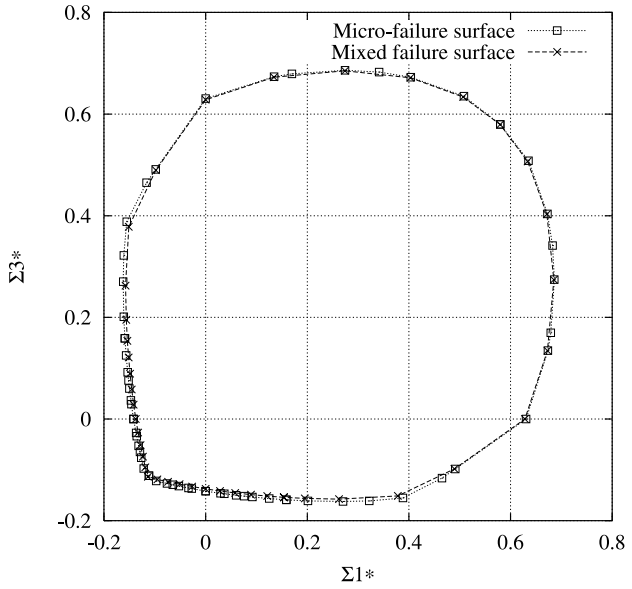

Fig. 14. Micro- and mixed failure surfaces in the $\Sigma_2 = 0$ plane.

In addition, in the uniaxial deformation and in the uniaxial compression, the obtained vectors $\underline{n}$ and $\delta\underline{\mathscr{U}}$ are respectively parallel and orthogonal to the loading direction: the localization band is thus shown to be a shear band.

Furthermore, we notice that $\delta\underline{\mathscr{U}}$ is zero for some loadings, which means that the mode is $C_{\min}$-periodic. Thus, in this case, the minimum unit cell is enough to predict buckling. As a result, the microfailure surface is achieved either for $C_{\min}$-periodic ($\underline{\omega} = 0$) or for long wavelengths ($\underline{\omega} \to 0$) eigenmodes (Figs. 15 and 16).

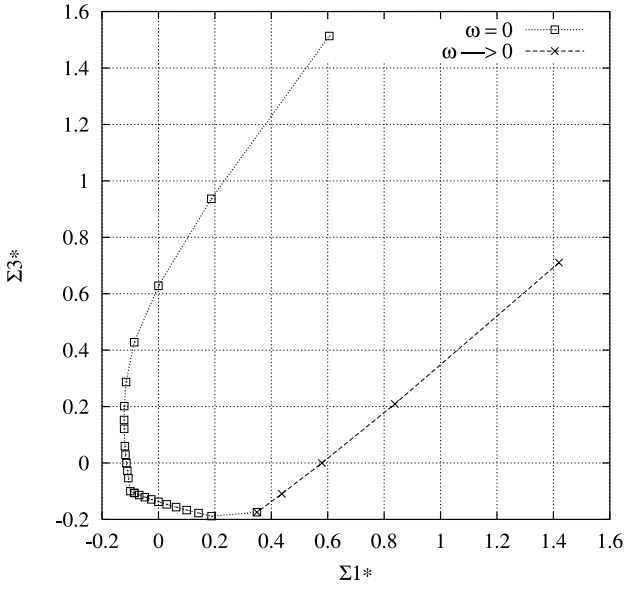

Fig. 15. Periodic and long wavelength modes surfaces in the $\Sigma_1 = \Sigma_2$ plane.

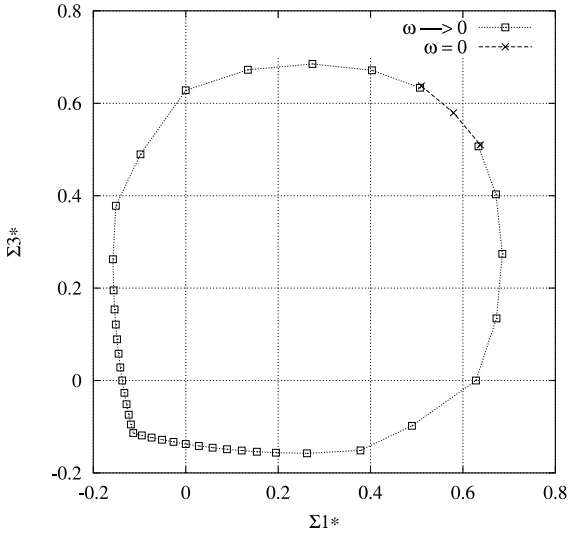

Fig. 16. Periodic and long wavelength modes surfaces in the $\Sigma_2 = 0$ plane.

4.5. A modified Drucker–Prager type failure surface

In order to extend our numerical results to proportional loading paths (2) with arbitrary $\underline{\underline{\tilde{E}}}$, we have tried to fit them with a modified Drucker–Prager type surface (Figs. 17 and 18). This model uses a failure surface which has an elliptic dependence of the deviatoric stress versus the pressure stress. In addition, this failure surface depends on the third invariant of the deviatoric stress.

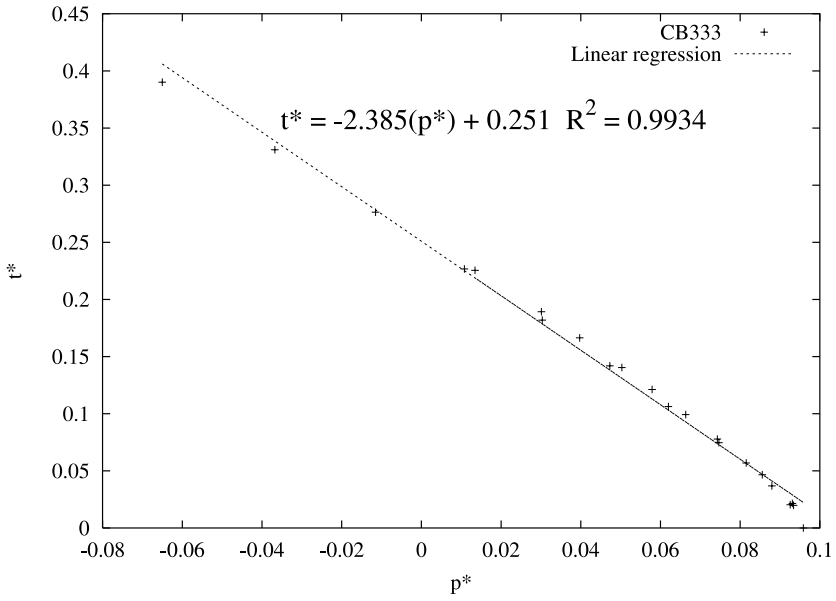

Fig. 17. Modified Drucker–Prager surface in the (p, t) plane.

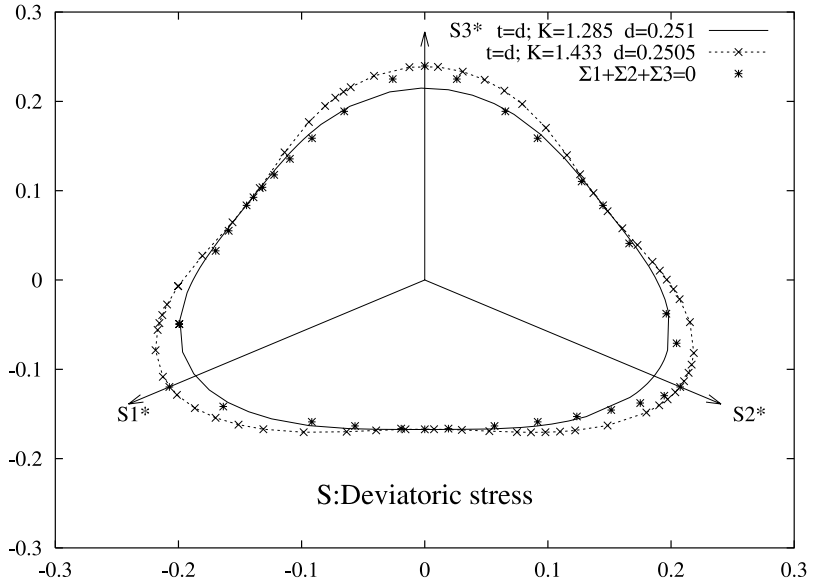

Fig. 18. Modified Drucker–Prager surfaces in the deviatoric stress space.

Actually, for p, q and r denoting respectively the equivalent pressure stress, the Mises equivalent stress and the third invariant of the deviatoric stress, we introduce a deviatoric stress measure, denoted by t, as follows:

$$t = \frac{q}{2}\left[1 + \frac{1}{K} - \left(1 - \frac{1}{K}\right)\left(\frac{r}{q}\right)^3\right], \tag{22}$$

where K is a material parameter,

$$p = -\frac{1}{3}\mathrm{tr}(\underline{\underline{\Sigma}}), \tag{23}$$

$$q = \sqrt{\frac{3}{2}\mathrm{tr}(\underline{\underline{S}} \cdot \underline{\underline{S}})}, \tag{24}$$

$$r = \left(\frac{9}{2}\underline{\underline{S}} \cdot \underline{\underline{S}} : \underline{\underline{S}}\right)^{1/3}, \tag{25}$$

and $\underline{\underline{S}}$ is the deviatoric stress

$$\underline{\underline{S}} = \underline{\underline{\Sigma}} + p\underline{\underline{I}}. \tag{26}$$

Notice that in uniaxial compression $t = q$ (as $(r/q)^3 = -1$). Whereas, in uniaxial tension $t = q/K$ (as $(r/q)^3 = 1$).

The modified Drucker–Prager surface is defined by

$$t - p\tan\beta - d = 0, \tag{27}$$

where β and d are material parameters.

In Fig. 18, two surfaces are presented: the best fitting convex surface (27) corresponding to $K = 1.285$ and a better fitting one, but resulting in a nonconvex surface (27), corresponds to $K = 1.433$.

4.6. Postbuckling analysis with nonsymmetrical modes

We remind that the plateau regime has not been exhibited by performing standard geometrically nonlinear analysis on relatively small unit cells (CB, CB3, etc.). Nevertheless, the introduction of an imperfection having the form of the first buckling mode allowed us to have, in a geometrically nonlinear analysis, stress–strain curves with a plateau regime corresponding to the critical load computed in the buckling analysis (see the curves denoted by "Nonlinear with imperfection" in Figs. 4 and 5). In addition, the scale effect of the buckling analysis is reproduced in the postbuckling analysis (Sab et al., 2000).

Moreover, without introducing any imperfection in the lattice structure, a standard geometrically nonlinear analysis has been performed on the very large unit cell CB333. Actually, due to the very large number of degrees of freedom, an instability occurred, leading to a plateau regime which corresponds to the critical load predicted in previous buckling analysis (Fig. 19). Notice that, due to this instability, the numerical calculations diverge at $E_{33} \simeq 15\%$ (Fig. 20).

4.7. Parametric study

4.7.1. Relative density

All the previous results have been conducted for a foam with relative density $R = 0.06$. As the range of relative density of interest is [0.02, 0.1], we have performed several buckling analyses with $R = 0.0254$ and 0.1. We have also performed buckling analyses with $R = 0.2$. We have presented the results in Fig. 21 in terms of the normalized stress $\underline{\underline{\Sigma}}^* = \underline{\underline{\Sigma}}/(E_s R^2)$. We notice that the three surfaces, corresponding to $R = 0.0254$, 0.06 and 0.1, coincide with a maximum relative error of 7.8%. Whereas, the relative density

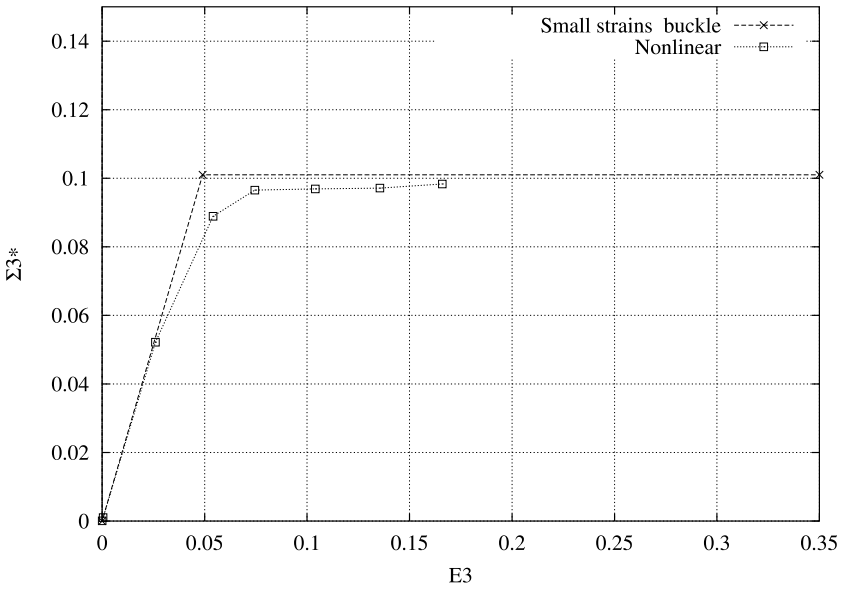

Fig. 19. Uniaxial deformation on CB333 stress–strain curves.

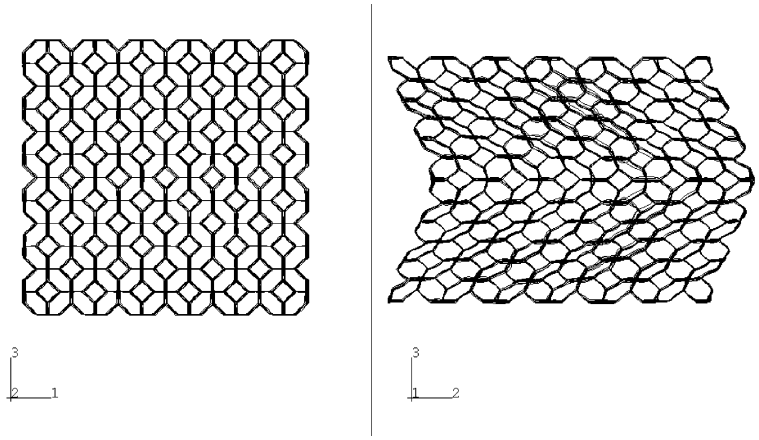

Fig. 20. Nonlinear mode of CB333 for uniaxial deformation.

$R = 0.2$ shows larger discrepancy. Therefore, it is reasonable to assume that in the range of density of [0.02, 0.1], the critical stresses are linearly dependent on R^2.

4.7.2. Euler–Bernoulli beams versus Timoshenko beams

We have performed all the numerical calculations with the Timoshenko beam model. However, the analytical formulae are usually performed with Euler–Bernoulli beams. In order to check their validity, we have performed some buckling analysis with Euler–Bernoulli beams. It is shown that in buckling analysis,

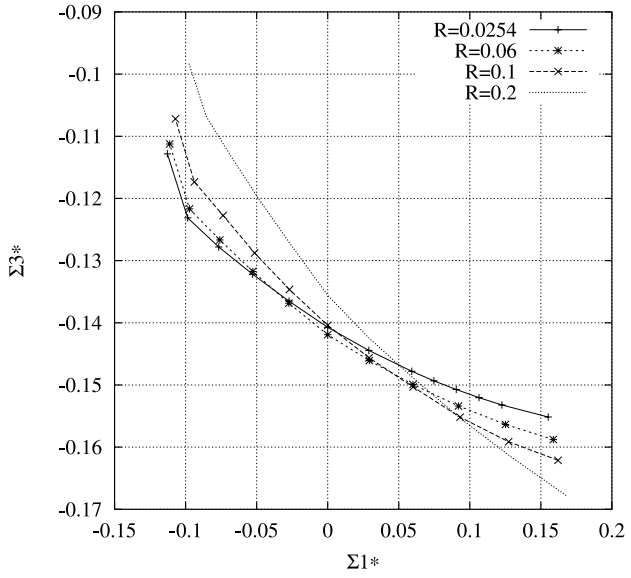

Fig. 21. Failure surfaces in the $\Sigma_2 = 0$ plane corresponding to different relative densities.

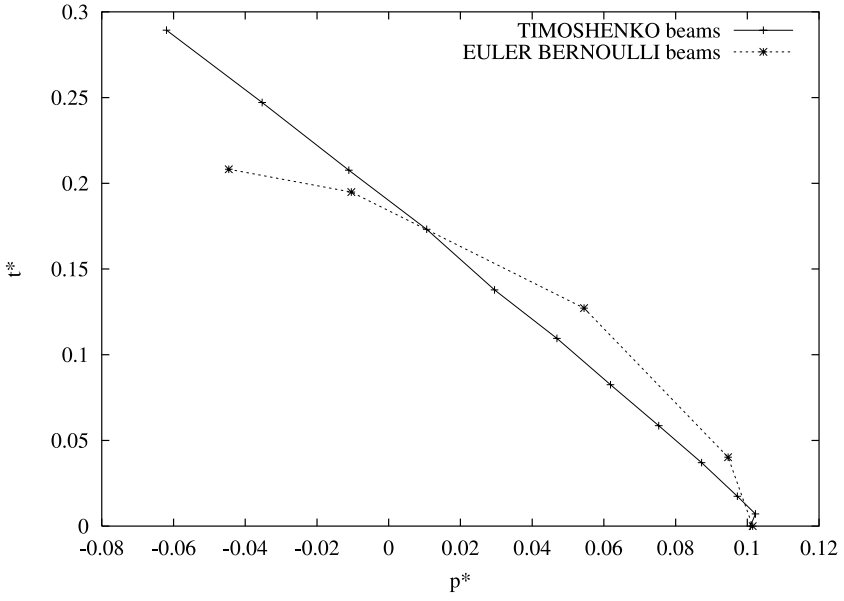

Fig. 22. Failure surfaces in the (p, t) plane corresponding to Euler–Bernoulli and Timoshenko beams.

Euler–Bernoulli beam assumptions give different results. Moreover, the modified Drucker–Prager surface does not fit well with these numerical results (Fig. 22). Actually, the Euler–Bernoulli beam assumptions are no more valid for relatively high relative densities.

5. Conclusions

We have presented the results of a numerical study on an infinite, perfectly periodic lattice with tetrakaidecahedral open-cells. More specifically, we have been interested in the prediction of the plateau regime exhibited by foams under high strain compression and allowing this class of materials to be used for energy absorption. It has been shown in the literature on honeycombs that this plateau regime is due to instabilities encountered during the loading. For this reason, we have focused first on the buckling analysis and then on the geometrically nonlinear behavior of the periodic beam lattice.

Buckling analyses have been performed by two different procedures and several loading paths. The first approach, termed periodic waves approach, consists in considering periodic eigenmodes on arbitrary unit cells. This leads to the critical load, λ_c^{micro}, defined as the infinimum of the critical loads of all possible unit cells. A second approach termed mixed approach has been defined. It consists in considering, on a minimum unit cell size Y, both periodic and nonperiodic eigenmodes depending on unit vectors $\underline{n}$. This leads to the critical load, denoted by λ_c^{mixed}, defined as the infinimum of the critical loads on all possible $\underline{n}$.

Considering the range of relative density of usual foams (i.e. [0.02, 0.1]), the cell edges of the tetrakaidecahedral lattice have been modeled by Timoshenko beams. The study of different unit cell sizes has shown that the minimum size representative unit cell is load dependent in buckling and in geometrically nonlinear analyses. Moreover, the two methods explained above led to the same failure surface. Actually, as in the study of Triantafyllidis and Schraad (1998) on honeycombs, we obtained a failure surface resulting either in Y-periodic or in long wavelength modes. This surface fits well with a modified Drucker–Prager surface.

Furthermore, unlike previous theoretical investigations on high strain compression of foams, we have obtained the plateau regime within two different ways.

The first one consists in considering a unit cell larger than the minimum unit cell, in order to be able to simulate some nonsymmetric deformation modes. This approach has been presented by Papka and Kyriakides (1994) for 2D honeycombs and has been extended here to a 3D periodic microstructure. An imperfection having the shape of the first buckling-type deformation mode has been introduced. A geometrically nonlinear analysis on the new imperfect periodic microstructure gives the plateau regime in the stress–strain curves.

The second method consists in considering a very large unit cell. Consequently, its high number of degrees of freedom allowed for a buckling-type deformation mode in a standard nonlinear analysis without introducing imperfection.

In conclusion, this study shows that using nonconvex homogenization and loss of stability theories, one can predict the behavior of a perfectly periodic lattice of elastic beams. Real foams are not perfectly periodic and can also exhibit material nonlinearities at the microscale. Experiments on real foams are being conducted in order to be compared to our numerical results.

Acknowledgements

We are grateful to Hibbitt, Karlsson and Sorensen, Inc. for making ABAQUS available under academic license.

Appendix A

The discretization of the microstructure has been decided through convergence studies. As a result, each edge has four B31 elements. The B31 beam element has one Gaussian integration point along its length and

17 integration points through the thickness of the elements, integrated by Simpson's rule, and providing sufficiently accurate results. This resulted in the table below:

Unit cell	Parallelipiped size	Nodes number	Elements number	Tetrakaidecahedra number in volume equivalence
C_{min}	(a,a,a/2)	91	48	1
CB	(2a,a,2a)	1936	512	8
CB3	(2a,a,6a)	5168	1472	24
CB5	(2a,a,10a)	7894	2432	40
CB333	(6a,6a,6a)	32160	22464	432

References

Abdelmoula, R., Krasucki, F., Marigo, J.J., 1994. Détermination de la charge de microflambage dans un composite. géme Journée Nationale sur les Composites, Saint-Etienne. 2, 731–740.

Gent, A.N., Thomas, A.G., 1963. Mechanics of foamed elastic materials. Rubber Chemistry and Technology 36, 597–610.

Geymonat, G., Müller, S., Triantafyllidis, N., 1993. Homogenization of nonlinearly elastic materials, microscopic bifurcation and macroscopic loss of rank-one convexity. Archive for Rational Mechanics and Analysis 122, 231–290.

Gibson, L.J., Ashby, M.F., 1982. The mechanics of three-dimensional cellular materials. Proceedings of the Royal Society of London A382, 43–59.

Gibson, L.J., Ashby, M.F., 1988. Cellular Solids: Structure and Properties. Pergamon Press, Oxford.

Gibson, L.J., Ashby, M.F., Schajer, G.S., Robertson, C.I., 1982. The mechanics of two-dimensional cellular materials. Proceedings of the Royal Society of London A382, 25–42.

Hilyard, N.C. (Ed.), 1982. Mechanics of Cellular Plastics. Macmillan Publishing Co., New York.

Maiti, S.K., Gibson, L.J., Ashby, M.F., 1984. Deformation and energy absorption diagrams for cellular solids. Acta Metallurgica 32, 1963–1975.

Marcellini, P., 1978. Periodic solutions and homogenization of nonlinear variational problems. Annali di Matematica Pura Ed Applicata 117, 139–152.

Müller, S., 1987. Homogenization of nonconvex integral functionals and cellular elastic materials. Archive for Rational Mechanics and Analysis 103, 189–212.

Nguyen, Q.S., 1995. Stabilité des structures élastiques. Springer-Verlag.

Papka, S.D., Kyriakides, S., 1994. In-plane compressive response and crushing of honeycomb. Journal of Mechanics and Physics of Solids 42, 1499–1532.

Papka, S.D., Kyriakides, S., 1998. Experiments and full scale numerical simulations of in-plane crushing of a honeycomb. Acta Materialia 46, 2765–2776.

Patel, M.R., Finnie, I., 1970. Structural features and mechanical properties of rigid cellular plastics. Journal of Materials 5, 909–932.

Pradel, F., 1998. Homogénéisation des milieux discrets périodiques orientés. Une application aux mousses. Ph.D. Thesis. Ecole Nationale des Ponts et Chaussées, Champs-sur-Marne.

Pradel, F., Sab, K., 1998. Cosserat modelling of elastic periodic lattice structures. Comptes Rendus de l'Académie des Sciences-Série IIB 326, 699–704.

Sab, K., Laroussi, M., Alaoui, A. 2000. Scale effects in high strain compression of periodic open cell foams. Twentieth International Congress of Theoretical and Applied Mechanics, ICTAM 2000, Chicago, 27 August–2 September.

Schraad, M.W., Triantafyllidis, N., 1997. Scale effects in media with periodic and nearly periodic microstructures, Part II: failure mechanisms. Journal of Applied Mechanics 64, 751–762.

Shaw, M.C., Sata, T., 1966. The plastic behavior of cellular materials. International Journal of Mechanical Sciences 8, 763–771.

Triantafyllidis, N., Bardenhagen, S., 1996. The influence of scale size on the stability of periodic solids and the role of associated higher order gradient continuum models. Journal of Mechanics and Physics of Solids 44, 1891–1928.

Triantafyllidis, N., Schnaidt, W.C., 1993. Comparison of microscopic and macroscopic instabilities in a class of two-dimensional periodic composites. Journal of Mechanics and Physics of Solids 41, 1533–1565.

Triantafyllidis, N., Schraad, M.W., 1998. Onset of failure in aluminium honeycombs under general in-plane loading. Journal of Mechanics and Physics of Solids 46, 1089–1124.

Warren, W.E., Kraynik, A.M., 1987. Foam mechanics: the linear elastic response of two-dimensional spatially periodic cellular materials. Mechanics of Materials 6, 27–37.

Warren, W.E., Kraynik, A.M., 1988. The linear elastic properties of open-cell foams. Journal of Applied Mechanics 55, 341–346.
Zhu, H.X., Knott, J.F., Mills, N.J., 1997. Analysis of the elastic properties of open-cell foams with tetrakaidecahedral cells. Journal of Mechanics and Physics of Solids 45, 319–343.
Zhu, H.X., Mills, N.J., Knott, J.F., 1997. Analysis of the high strain compression of open-cell foams. Journal of Mechanics and Physics of Solids 45, 1875–1904.